Tectonophysics 839 (2022) 229551

Contents lists available at ScienceDirect

Tectonophysics

journal homepage: www.elsevier.com/locate/tecto

Hot lithosphere beneath the northeastern North China Craton detected by ambient noise tomography

Lixue Ma [a,d], Tao Xu [a,c,*], Yinshuang Ai [b,c,*], Jinhui Yang [a,c], Yingjie Yang [e], Enbo Fan [a,d], Long Li [a,d], Jue Hou [a,d,f], Weiyu Dong [a,d]

[a] State Key Laboratory of Lithospheric Evolution, Institute of Geology and Geophysics, Chinese Academy of Sciences, Beijing 100029, China
[b] Key Laboratory of Earth and Planetary Physics, Institute of Geology and Geophysics, Chinese Academy of Sciences, Beijing 100029, China
[c] Innovation Academy for Earth Science, CAS, Beijing 100029, China
[d] University of Chinese Academy of Sciences, Beijing 100049, China
[e] Department of Earth and Space Sciences, Southern University of Science and Technology, Shenzhen, Guangdong 518055, China
[f] Institute of Geophysics, China Earthquake Administration, Beijing 100081, China

ARTICLE INFO

Keywords:
North China Craton
Ambient noise tomography
Crustal velocity structure
Thermal state of lithospheric mantle

ABSTRACT

In this study, we present a high-resolution, 3-D S wave velocity (Vs) model of the crust and uppermost mantle beneath the Liaodong area at the northeast margin of the North China Craton (NCC). We build the model based on ambient noise tomography. Ambient noise data were obtained from both permanent stations and two new broad-band station profiles covering the Dandong-Tongliao (NCISP-10) and Baishan-Kuandian (NCISP-11) areas of the Liaodong-jilin region from October 2016 to December 2019. Our model reveals that different sides of the Tanlu Fault exhibited different Vs anomalies in both the upper crust and lithospheric upper mantle. Low Vs anomalies are observed in the west of the Tanlu Fault, which are interpreted to represent compositional variations at the crustal level. On the eastern side, low Vs anomalies are imaged which appear to represent "heat" or "hot material" derived from the deep mantle. A high Vs anomaly imaged in the southwest of the Songliao basin spatially coincides with a geologic feature referred to as the southwest uplift, which divides the basin into two secondary depressions. The Vs anomaly is inferred to represent cold mafic magma produced by the subduction of the Pacific Plate during the Late Cretaceous. Upwelling of mantle materials provide the best explanation for a mass of hot lithosphere. They underplated at the base of the crust, which formed crustal reservoirs and was eventually emplaced as plutons or erupted as volcanic rocks observed around the study area.

1. Introduction

Griffin et al. (2003) proposed a coupled crust-mantle system in which the same tectonic thermal event can simultaneously affect both the continental crust and the lithosphere. This paradigm states that there are three types of the sub-continental lithospheric mantle (SCLM) including Archean SCLM (> 2.5 Ga), Proterozoic SCLM (2.5–1.0 Ga) and Phanerozoic SCLM (< 1.0 Ga). O'Reilly and Griffin (2006) suggested that these three types of lithosphere differ in terms of their thermal state and thickness. Archean SCLM is the coldest (35–40 $W \bullet m^{-2}$) and thickest (180–240 km) followed by Proterozoic SCLM (40–45 $mW \bullet m^{-2}$, 150–180 km). Phanerozoic SCLM represents the warmest (> 50 $mW \bullet m^{-2}$) and thinnest (60–140 km) lithosphere. Northeast China consists of the northeast part of the North China Craton (NCC) and the eastern part of the Central Asian Orogenic Belt (CAOB). Nd isotopic data indicates the crustal formation ages of the two blocks are about 2500–2800 Ma and 600–1000 Ma, respectively, while Os T_{RD} model ages of mantle xenoliths reveal both Proterozoic and Phanerozoic model ages of the underlaying SCLM (Wu et al., 2003). According to the classification of the three types of lithosphere proposed by Griffin et al. (2003) and O'Reilly and Griffin (2006), the Proterozoic and Phanerozoic SCLM beneath the northeast of NCC and the east of CAOB should be relatively thin and exhibit high temperatures. The thermal state of lithosphere determines its rheology and physical properties, which influences tectonic deformation and overall geological evolution in the long term and also affects the velocity and attenuation of seismic wave propagation. Therefore, we used seismic wave velocities to inquire about the thermal state of the NCC and CAOB and constrain the crust-mantle evolution of

* Corresponding authors at: Institute of Geology and Geophysics, Chinese Academy of Sciences, Beijing 100029, China.
E-mail addresses: xutao@mail.iggcas.ac.cn (T. Xu), ysai@mail.iggcas.ac.cn (Y. Ai).

https://doi.org/10.1016/j.tecto.2022.229551
Received 30 September 2021; Received in revised form 7 August 2022; Accepted 24 August 2022
Available online 28 August 2022

these two regions.

In recent years, geological and geochemical researches have not only presented the fine process of magma underplating the lower crust (Tang et al., 2013), but also established a set of sequences of surface responses such as multi-stage magmatic activity (Tang et al., 2018; Zhang et al., 2014), extensional dome and metamorphic core complex formation (Liu et al., 2013; Wang et al., 2013; Zhang et al., 2012) and extensional faults and basin groups in Northeast China (Li et al., 2007; Meng et al., 2003; Song et al., 2018; Song et al., 2014; Wang et al., 2013; Zhu et al., 2012). Compared to the detailed analysis of lithospheric activation processes, the velocity structure of the crust and lithospheric mantle associated with different thermal states remains enigmatic.

Several models have been proposed to explain the mantle dynamics in Northeast China. For example, two contrasting models seek to explain the origin of the Changbai volcanoes (CBV). The first model suggested by Lei and Zhao (2005) proposed that the Changbai intraplate volcanism originates from flux melting of the upper mantle wedge, caused by the dehydration of the Pacific plate which is stagnated in the mantle transition zone (MTZ). A second model proposed by Tang et al. (2014) suggested that a low-velocity gap within the stagnant Pacific slab in the MTZ beneath Northeast China facilitated the upwelling of entrained sublithospheric mantle beneath the stagnant Pacific slab and the decompression melting of the upwelling mantle feeds the Changbai volcanoes. Recently, Guo et al. (2018) also suggested that small-scale mantle convection could explain the origin of the CBV. Although these models vary, numerous studies have provided a detailed picture of crustal and lithospheric structure beneath Northeast China (Guo et al., 2015; Guo et al., 2016; Liu et al., 2017).

Tomographic imaging has recently benefitted from advances in seismic imaging based on dense seismic arrays. Dense seismic arrays have significantly improved the imaging of crust-mantle structure. For example, Zheng et al. (2015) used the P wave receiver function method to acquire crustal interface information using dense array profiles covering southern Liaoning, the Tanlu Fault Zone (TLFZ), the southern margin of the Songliao Basin (SLB), the Solun suture zone and the CAOB. They detected active tectonic and magmatic events at a crustal scale and linked them to the Late Mesozoic extensional history of the NCC. Fan and Chen (2019) analyzed seismic records from dense seismic arrays and permanent stations in Northeast China to image 3-D crustal and lithospheric S wave velocity structures. They detected a CBV magma chamber in the lower crust and proposed a model for the evolution of the crust-mantle magmatic system. In this study, we used two new portable seismic station profiles combined with surrounding permanent stations to analyze the thermal state of the crust and uppermost mantle beneath the northeast NCC and the SLB.

2. Geological setting

Northeast China includes the northeast part of the NCC and the eastern part of the CAOB. The Solun suture zone separates these two areas with the NCC to the south and the CAOB to the north (Fig. 1). As the eastern part of the CAOB, the Xing'an Mongolian Orogenic Belt (XMOB) is composed primarily of granites showing relatively young Nd T_{DM} model ages (0.6–1.0 Ga) (Jahn et al., 2000; Wu et al., 2002). The NCC is one of the oldest continental cores and has crustal rocks as old as 3.8 Ga (Liu et al., 1992). Felsic rocks of the NCC have Archean (2.5 and 2.9 Ga) Nd T_{DM} model ages (Wu et al., 1997).

Since the late Mesozoic, Northeast China has experienced major tectonic-magmatic events caused by the subduction of the Paleo-Pacific plate (Wu et al., 2003). The far-field effects of the subduction include intensive deformation, mineralization and magmatism (Wang and Mo, 1995) which generated intermediate-acid volcanic rocks and emplaced granites over a widespread area. Subduction also created a series of large-scale rift basins including the Songliao and Bohai Bay basins (Meng et al., 2003; Zhu et al., 2012) that controlled by the Tanlu Fault (Zhu et al., 2012). During Late Cretaceous rifting, the Songliao Basin received up to 6 km thick fluvial-lacustrine sediments (Feng et al., 2010; Song et al., 2014; Wang et al., 2013).

Major Cenozoic events include extensive eruption of volcanic rocks. Basaltic rocks primarily comprise earlier subalkalic and alkalic basalts

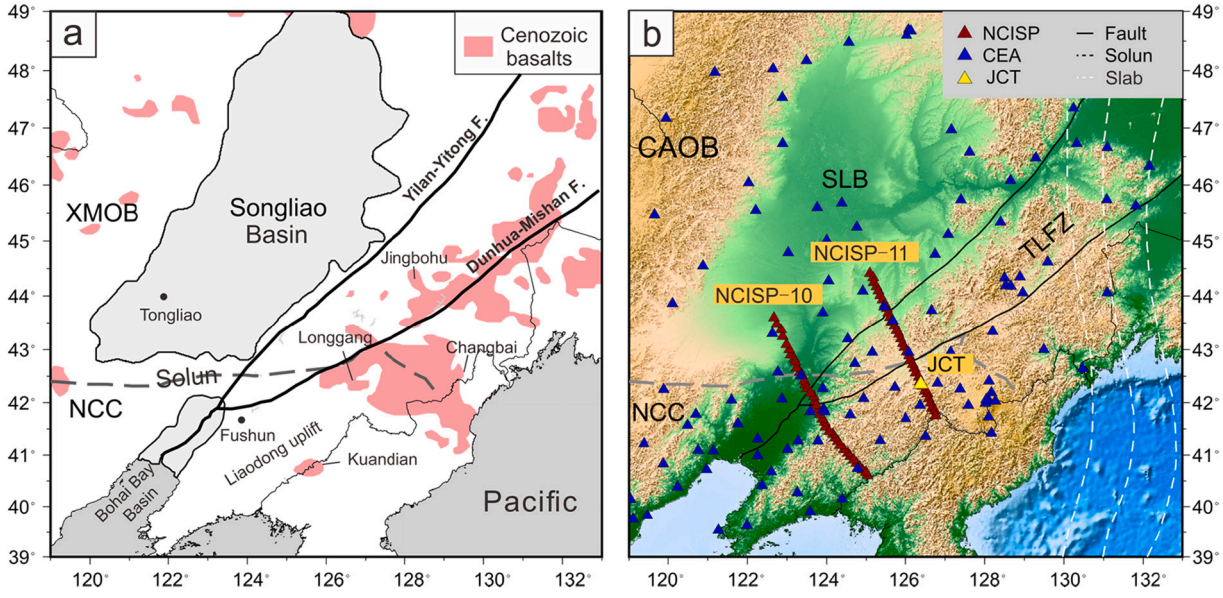

Fig. 1. (a) Simplified tectonic map of northeast China, showing spatial distribution of Cenozoic (green) basalts. The Tanlu Fault Zone is marked by black lines, including northern part of Yilan-Yitong fault (YYF) and southern part of Dunhua-Mishan fault (DMF). Four main volcanic fields in the study area: Kuandian (KD), Longgang (LG), Changbai volcano (CBV), Jingbohu (JBH). Cities of Tongliao and Fushun (FS) refferred to in the text are marked in black dots. The Xing'an Mongolian Orogenic Belt (XMOB) is the eastern part of the Central Asian Orogenic Belt (CAOB). (b) A map showing NCISP array and CEA national permanent seismic stations. Solid black lines represent the Tanlu fault zone. Dashed grey lines show Solun suture zone. The abbreviations in this figure are as follows: North China Craton (NCC), Central Asia Orogenic Belt (CAOB), Songliao Basin (SLB), Changbai Mountain Range (CMR), and Tan-Lu Fault Zone (TLFZ). NCISP = North China Exploration Seismic Profile; CEA = China Earthquake Administration. Station JCT marked in yellow is used to plot the cross-correlation records in Fig. 2. (For interpretation of the references to colour in this figure legend, the reader is referred to the web version of this article.)

and later minor continental-type tholeiites as well as ultramafic alkali basalts (Fan and Hooper, 1989; Liu et al., 1995). These rocks indicate that Cenozoic magmatism favored alkali enrichment.

3. Data processing

3.1. Seismic data

The study area spanned from 39°N to 47°N in latitude and from 119°E to 130°E in longitude (Fig. 1). We collected continuous vertical-component seismograms from two portable arrays and one permanent network in China. There are 72 portable stations from the two profiles of NCISP-10 and NCISP-11 (North China Exploration Seismic Profile) and 98 permanent stations from China Earthquake Administration (CEA) network (Zheng et al., 2010). The NNW-SSE trending NCISP-10 profile traversed the TLFZ and the SLB in eastern Liaoning and operated from October 2016 to July 2018, consisting of 38 seismic stations spanning a total length of 370 km with an average interstation distance of 10 km. A parallel broad-band dense array named NCISP-11 was deployed in the Jilin area from July 2018 to December 2019, including 34 seismic stations spanning a total length of 340 km with an average station spacing of 10 km. Since the two seismic arrays were asynchronously deployed, no cross-correlations between these two profiles were generated, and they were cross-corelated with synchronous CEA stations independently.

3.2. Ambient noise tomography

Following the methods described in Bensen et al. (2007) and Yang et al. (2007), we perform cross-correlation using ambient noise data. Vertical components of continuous raw seismic seismograms were cut to daily segments at 5 Hz. All of them were then band-pass filtered at the period band of 3–80 s after instrument responses were removed. We then applied temporal normalization and frequency domain spectrum whitening to suppress the influences of large earthquakes and balance the frequency band range of ambient noise (Yang et al., 2007). Afterwards, we performed cross-correlation between the pre-processed daily seismograms. Finally, we linearly stacked all the daily cross-correlations between individual station pairs to obtain stacked cross-correlations.

Fig. 2a and b show examples of cross-correlations between station JCT (yellow triangle in Fig. 1b) and all other stations. Coherent signals appear clearly at both positive and negative time lags. We stacked the positive and negative lags of the cross-correlations to improve the signal-to-noise ratio (SNR) (Bensen et al., 2007). We then performed automatic time-frequency analysis (AFTAN) (Levshin and Ritzwoller, 2001) based on multiple filters and phase-matched filters to measure phase velocity dispersion curves. The grey curves in Fig. 3a and b show all the dispersion curves obtained by the AFTAN method. The black curves represent the dispersion curves retained after a series of quality control steps. We applied the following data selection criteria to the dispersion curves to discard some low-quality dispersion curves. Firstly, we calculated SNR of surface waves in each cross-correlation following Bensen's definition and only retained measurements with SNR larger than ten. Secondly, measurements with interstation distances less than two wavelengths were discarded. Thirdly, dispersion measurements with phase velocities greater than three times the standard deviation of phase velocities from all dispersion measurements were discarded. Finally, we calculated the residual of phase travel times for each station pair following a method described in Yao et al. (2010). Station pairs with residuals >5 s were discarded. The red circles in Fig. 3a and b represent the numbers of ray paths in the corresponding period retained after the quality control steps. To improve resolution and stability, we combined the dispersions of NCISP-10 and NCISP-11 for subsequent phase velocity inversion.

4. Phase velocity maps

Based on the assumption of great-circle path propagation of the surface wave, we used a regionalized imaging method developed by Montagner and Nataf (1986) to invert the retained dispersion curves for phase velocity maps. The inversion is to minimize the following objective function:

$$\varnothing(\boldsymbol{m}) = [\boldsymbol{t}(\boldsymbol{m}) - \boldsymbol{t}_{obs}]^T \boldsymbol{C}_D^{-1} [\boldsymbol{t}(\boldsymbol{m}) - \boldsymbol{t}_{obs}] + (\boldsymbol{m} - \boldsymbol{m}_p)^T \boldsymbol{C}_M^{-1} (\boldsymbol{m} - \boldsymbol{m}_p) \quad (1)$$

where $\boldsymbol{m}$ and $\boldsymbol{m_p}$ are vectors for inverse and prior slowness models, $\boldsymbol{t}$ and $\boldsymbol{t}_{obs}$ are vectors of calculated and observed traveltimes. The $\boldsymbol{C_D}$ is the data covariance matrix describing the data uncertainties and related to the measurement error of dispersions (σ_d). According to previous study of the dispersion measurements (Yao et al., 2010), we set the standard error σ_d of all measured dispersions to 1.5%. The $\boldsymbol{C_M}$ is the prior model covariance function between model estimates at $\boldsymbol{r}_1$ and $\boldsymbol{r}_2$ which are usually chosen as the Gaussian functions (Montagner and Nataf, 1986; Yao et al., 2010).

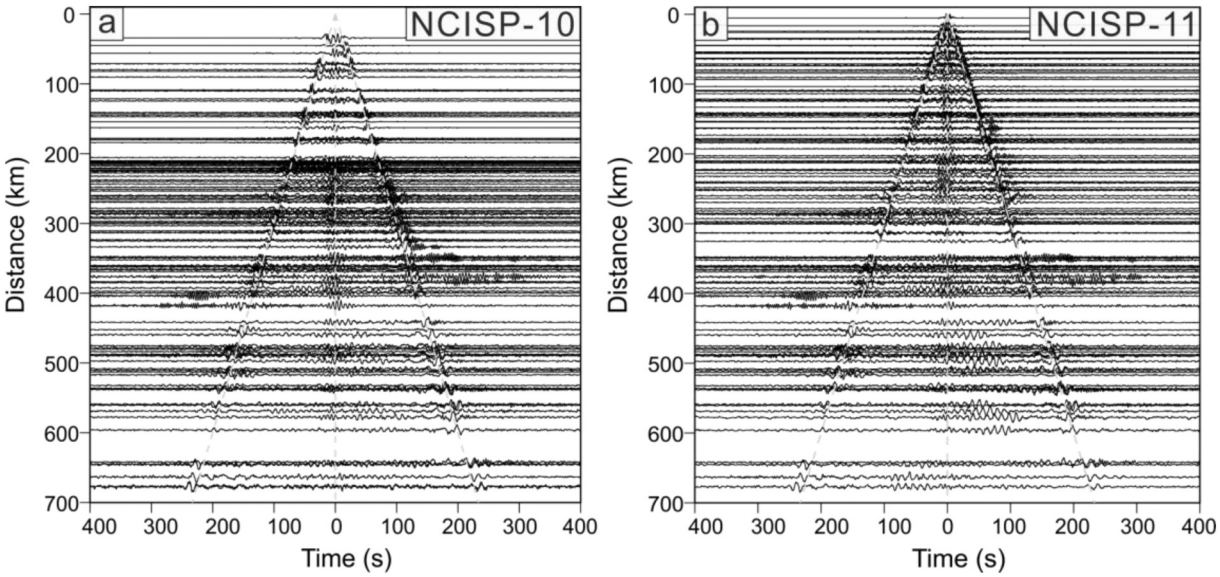

Fig. 2. Cross-correlations of station pairs of station JCT with those from (a) NCISP-10 and from (b) NCISP-11, respectively.

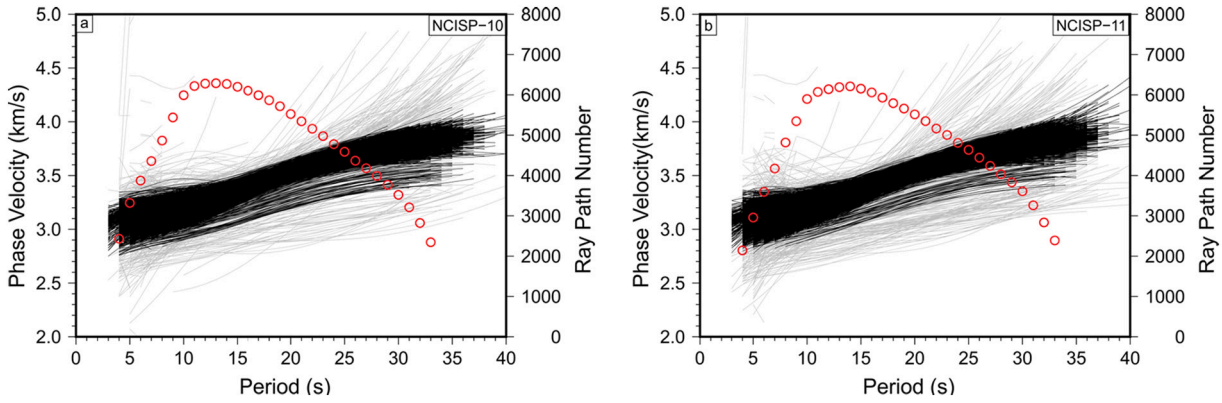

Fig. 3. Rayleigh wave phase velocity dispersion measurements among station pair in NCISP-10 (a) and in NCISP-11(b), respectively. Grey lines represent dispersion curves acquired by the automatic frequency-time analysis method between all station pairs before quality controls. Black thin lines show the retained dispersion curves after all the quality controls. Red circles are the number of the retained dispersion curves. (For interpretation of the references to colour in this figure legend, the reader is referred to the web version of this article.)

$$\boldsymbol{C_M}(r_1, r_2) = \sigma_m^2 e^{-(r_1-r_2)^2/2L^2} \tag{2}$$

$$\sigma_m = \sigma_p / v_0^2 \tag{3}$$

where σ_m represents the prior model errors, v_0 is the initial velocity which is set to be the average dispersion measurements at each period. The prior velocity error (σ_p) and the correlation length (L) control the amplitude of anomalies and smoothness of inverted models, respectively. The correlation length (L), determined by path coverage and wavelengths (Griot et al., 1998), was set to one wavelength with a minimum value of 40 km and a maximum length of 120 km. The optimal prior velocity error (σ_p) was used to optimize tradeoffs between model norm and data-variance reduction for each period. According to the trade-off curve in Fig. 4a, we then set the prior velocity error σ_p to 0.12 km/s. The overall travel time residuals of the final inversion at period 20 s are given in Fig. 4b. The misfits show a Gaussian type distribution centered near zero with a small standard deviation (0.82 s) as indicated in Fig. 4b. The inversion has removed unrealistic measurements and significant outliners.

We performed a traditional checkerboard test with an anomaly size of 1 ° × 1° and 8% velocity perturbations relative to an average phase velocity of 4.0 km/s to estimate inversion resolution. We added 1% Gaussian random noise to synthetic phase velocities. The recovered models from the checkerboard resolution test are plotted in Figs. 5a-c, showing that the phase velocity perturbations are clearly recovered at periods of 10 s, 20 s and 30 s. Figs. 5d-f show the ray path coverage density for periods of 10 s, 20 s and 30 s respectively.

Phase velocities at different periods show sensitivities to the S wave velocities at different depth ranges (Fig. 6). Rayleigh wave phase velocities at shorter periods (4–15 s) are sensitive to the structure of the upper and middle crust (5–20 km), while phase velocities at intermediate periods (20–33 s) show sensitivities to the lower crust and the uppermost mantle (≥25 km). Based on the inversion method mentioned above, we obtained a 2-D Rayleigh wave phase velocity map. Fig. 7 shows phase velocity maps plotted as perturbations to the averages plotted on the top right of each panel for periods of 5 s, 10 s, 15 s, 20 s, 25 s and 30 s.

The phase velocities of 4–15 s periods (Figs. 7a-c) outline the characteristics of the velocity structure of the upper and middle crust. The east and west sides of the TLFZ clearly show different velocity structures. The SLB exhibits a low-velocity anomaly, whereas a high-velocity anomaly clearly appears beneath the Changbai Mountain Range and eastern Liaoning. Compared with the Longgang volcano (LGV), the Changbai volcano (part of the CBV) exhibits a low-velocity anomaly, and as the period increases, the range of low-velocity anomaly extended

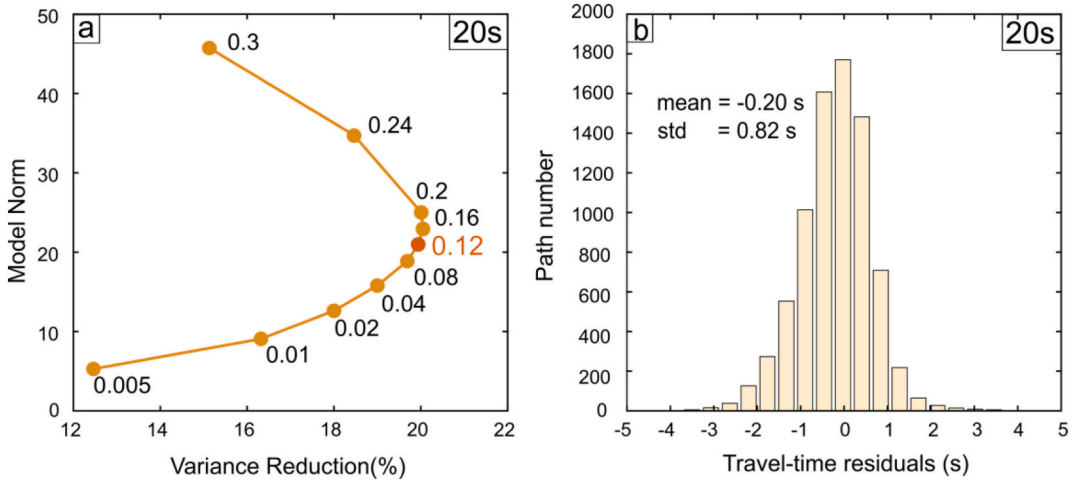

Fig. 4. (a) L-curve of trade-off between model norm and data deviation reduction at periods of 20 s. Yellow solid circles represent different values of the prior velocity error (σ_p). The best value shown in orange is 0.12 km/s. (b) Histogram of traveltime residuals at period 20 s after the final inversion. The mean value and standard deviation of the residuals are indicated inside in the panel. (For interpretation of the references to colour in this figure legend, the reader is referred to the web version of this article.)

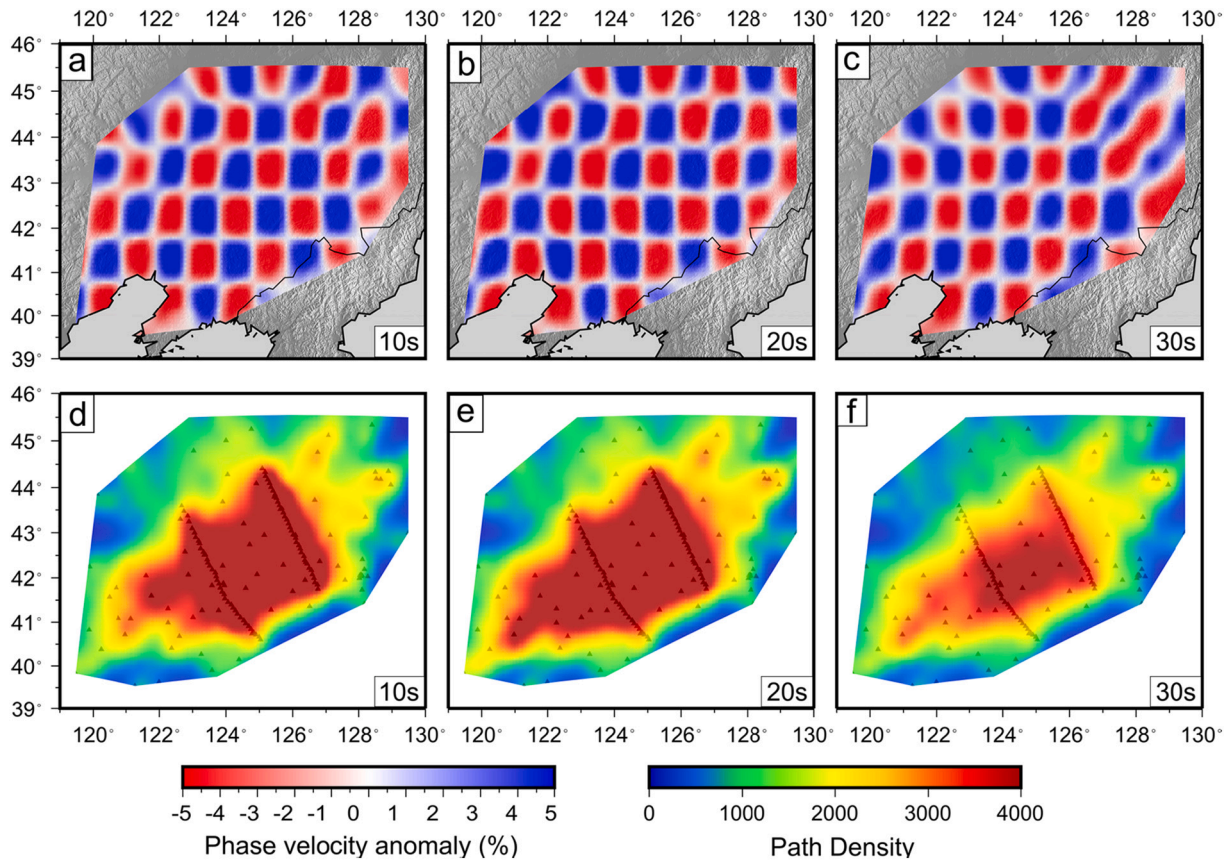

Fig. 5. Checkboard resolution tests for ambient noise tomography and ray path coverage densities. The checkboard input model with anomaly sizes of 1 ° × 1°. The magnitudes of the input anomalies are ±0.8 km/s. (a-c) The recovered models at 5 s, 10 s, and 30 s respectively. (d-f) The corresponding ray path coverage for each period.

gradually. The phase maps (Figs. 7d-f) of periods of 20 s and 30 s mainly show the velocity of the lower crust and uppermost mantle. Short period images indicate opposing geological characteristics for the east and west sides of the TLFZ. The east side of the TLFZ shows large-scale, low-velocity features, while the west side of the TLFZ shows large-scale, high-velocity characteristics. Both the CBV and LGV are connected with low-velocity anomalies. In contrast, the amplitude and range of low-velocity anomalies in the SLB are weaker and smaller with increasing period.

5. S Wave velocity structure

5.1. Inversion method

We extracted the pure path dispersion curves at each geographic point from the phase velocity maps and then inverted the pure path phase velocity dispersion curves for 1-D S wave velocity using a linear inversion method (Herrmann, 2013). Considering the period range of 4–33 s of the phase velocities, we set the input model from the surface down to 80 km. This model was parameterized with a grid of 0.5 ° × 0.5° in the horizontal dimension and with layers' thickness varying from 1 km at the upper 5 km of crust to 2 km at the upper 40 km depth to 5 km at 40–80 km depths. We extracted the 3-D S wave velocity model of Shen et al. (2016) as the initial model. To minimize the bias from the dependence of the inversion on the initial velocity, we followed the previous inversion strategy of Fan and Chen (2019). This procedure uses the reference velocity model as an input to generate 200 models randomly and uniformly with a maximum Vs perturbation of 5% at each layer (Fig. 8a). The linear inversion method (Herrmann, 2013) was then applied to the 200 perturbed input models at each grid.

Because surface waves are sensitive to structures at ranges of depths, they cannot provide good constraints on the velocity discontinuity. Here we used previous results of H-κ analysis (He et al., 2014; Tao et al., 2014; Dong et al., 2022) to constrain the Moho depth and the velocity ratio, V_P/V_S, within the crust. The P wave velocity was calculated according to the initial S wave velocity model and V_P/V_S. The density structure was determined according to the empirical formula $\rho \approx 1.77 + 0.2V_P$ (Nafe and Drake, 1957).

Fig. 8 shows examples of one-dimensional S wave velocity model for the SLB (Fig. 8b), the CBV (Fig. 8c) and the Fushun (Fig. 8d). Their geologic locations are plotted in Fig. 7f. The solid red line represents the average velocity of the 200 inverted models. The grey part represents two standard deviations of the 200 final inverted models. The inset map shows the predicted phase velocities (red line) from the best fitting mean model compared with the dispersion observations (black line). It can be seen that the predicted dispersion from the inverted S wave velocity fits well with the observed dispersion curve (Figs. 8b-8d).

5.2. S wave velocity (Vs) structure

Finally, we assembled all the 1-D S wave velocities to obtain a 3-D Vs model of the study region. Fig. 9 displays Vs perturbations at different depths. The Vs perturbations are shown relative to the average velocity at the corresponding depth. In the shallow crust (Figs. 9a-b), Vs is highly related to the geological structures at the surface. The SLB and Bohai Bay basin show a significantly low Vs, while the TLFZ and the Changbai Mountain Range display a high Vs. The upper crust of the CBV manifests itself as a minor, local Vs anomaly, and the middle and lower crust is characterized as a significant Vs anomaly. As shown in Figs. 9d-f, a notable banded Vs anomaly appears at the top of the lower crust and upper mantle in the Fushun area near the TLFZ. At greater depths, the

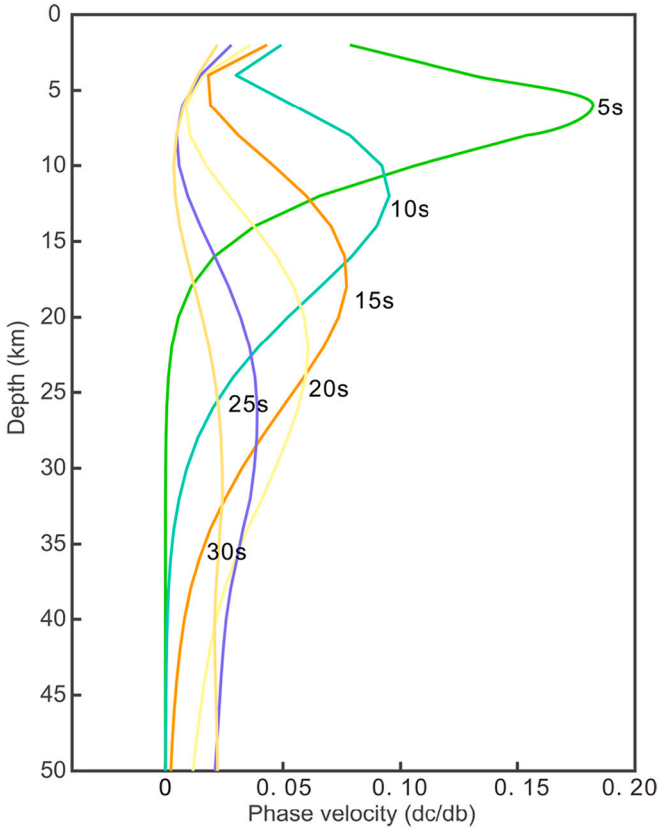

Fig. 6. Sensitivity kernels of Rayleigh waves at specific periods of 5 s, 10 s, 15 s, 20 s, 25 s, and 30 s.

low-velocity zone appears to be connected with the LGV and CBV. Around the SLB, a high Vs anomaly appears at the top of the upper mantle. Guo et al. (2018) performed a joint tomography of surface and body waves to reveal that the high Vs of the upper mantle beneath the SLB extends to >200 km depth.

Fig. 10 shows four vertical cross sections with their profiles delineated in Fig. 9f. Profile AA′ traverses the Fushun and CBV, while BB′ spans the entire SLB to the NE direction. AA′ shows distinct low Vs anomalies beneath the Fushun and CBV in the upper mantle. The two anomalies merge in the upper mantle (Fig. 10a). The crust beneath the SLB exhibits an obvious ups and downs pattern of velocity variations which resembles the Kailu sag, the southwestern uplift and the central depression (Fig. 9a, Fig. 10b). Also, the upper mantle beneath the SLB is imaged as a relatively high Vs anomaly (Fig. 10b). Fig. 10c and d display the Vs transects along the two profiles of NCISP-10 and NCISP-11. Both of them display high velocity upper mantle beneath the SLB (west of the TLFZ) and low velocity upper mantle beneath the NCC (east of the TLFZ). We also performed inversions along profiles NCISP-10 and NCISP-11 independently. Comparisons between transects from 3-D Vs map and from 1-D tomography are imaged in Fig. S1.

The crustal structures in this study coincide with observed surface geological structures and consistent with previous work (e.g., Fan and Chen, 2019; Guo et al., 2015; Guo et al., 2016; Liu et al., 2017). For the middle crust beneath the SLB, our results identified a high Vs anomaly associated with the southwestern uplift. This feature was also reported from ambient adjoint tomography by Liu et al. (2017). A number of studies have reported low Vs anomalies in the middle to lower crust and uppermost mantle beneath the Fushun and CBV (e.g., Chen et al., 2007; Fan and Chen, 2019; Guo et al., 2016; Zhang et al., 2019; Zhao and Tian, 2013). The TLFZ seems to separate the SLB and NCC into two parts within the upper crust and upper mantle (Figs. 9a-b, Figs. 9e-f, Figs. 10c-d).

6. Discussion

6.1. Contrasting Vs structure beneath the crust and mantle on the east and west sides of the TLFZ

Our 3-D Vs model shows that the velocity structure of the study area differs on both sides of the TLFZ. Generally, the east side is characterized by high crustal velocities and the west side by low velocities (Figs. 9a-b). The top of the upper mantle however displays velocity patterns opposite to those appearing in the upper and middle crust, with high velocities in the west and low velocities in the east (Figs. 9e-f). At more local scales, high middle and lower crustal Vs domains occur interspersed with low Vs anomalies in the east (Figs. 9c-d). While, the typical low Vs domains are separated by a high Vs anomaly in the west (Figs. 9c-d).

The SLB rests on the west side of the fault and hosts thick accumulations of Mesozoic to Cenozoic sediments. These appear as a low Vs anomaly. Similarly, Cenozoic sediments are accumulated in the Bohai Bay Basin (BHB). These also show a low Vs anomaly (Fig. 9a). The east side of the fault exposes areas of basic rocks including ridge, Longgang Mountain and Changbai Mountain. These appear as a high Vs anomaly. Contrasts in physical properties of materials on either side of the TLFZ thus contribute to the observed velocity differences.

The low velocity structure in the eastern upper mantle and high velocity in the western upper mantle likely reflects higher mantle temperatures in the east. Temperature, rock composition, melts and other fluids can all affect seismic wave velocity. Petrologic analysis of peridotite xenoliths from Cenozoic basalts in Northeast China found low water content in the lithospheric mantle (Hao et al., 2016). Meanwhile, Karato (2011) argued that water content does not strongly influence seismic wave velocities, which instead relies on other factors such as major element compositions and temperature. The increase of a $100°C$ in temperature would decrease in S wave velocity between 0.7 and 4.5% (Goes et al., 2000). In contrast, variations in composition inferred from mantle xenoliths usually give changes in velocity smaller than 1% (Goes et al., 2000). The present temperature from mantle xenoliths in the west part of the TLFZ is $\sim 850°C$ - $950°C$, lower than that estimated for the eastern part of the TLFZ ($900°C$ - $1141°C$) (Yu et al., 2007). Intuitively, low Vs anomalies detected for the eastern upper mantle correspond to low Vs anomalies detected within the crust, which spatially overlap with the general distribution of Cenozoic volcanic rocks and features (Fig. 1a, Figs. 9e-f). Thus the "hot" upper mantle on the eastern side of the TLFZ may arise from the addition of mantle-derived magma and deeper heat sources.

Although the low Vs anomaly in the upper mantle on the east side of the TLFZ roughly corresponds to the spatial location of the low-velocity anomaly at the crustal level, the scale and intensity of the anomaly gradually weakens from the upper mantle to the upper crust. This pattern is consistent with thermal decay of a hot body extending from the upper mantle to the upper crust. Meanwhile, the low Vs anomaly in the SLB weakens gradually from the upper to the lower crust and appears only weakly at the top of the upper mantle. Thus the low-velocity anomalies behave differently on either side of the TLFZ. Anomalies appear to represent variation in composition at crustal levels on the western side of the fault, while represent thermal variation arising from the deep mantle on the eastern side of the fault.

Here, we revealed the contrasting S wave velocity anomalies of the lithospheric mantle on either side of the TLFZ. On the western side of the TLFZ, the lithospheric mantle exhibits as a high Vs anomaly and has low geothermal temperature. On the east of the TLFZ, the lithospheric mantle shows as a low Vs anomaly and has higher geothermal temperature. The study of Meng et al. (2021) suggested that the lithosphere-asthenosphere boundary is shallower within the NCC, with a depth of ~110 km, while in the southern SLB it reaches about 130 km. The degree of lithosphere thinning (~80 km thinning) of the NCC is greater than that in the SLB. This may explain why the geothermal gradient of the lithosphere in the NCC is higher than that in the SLB and the lithosphere

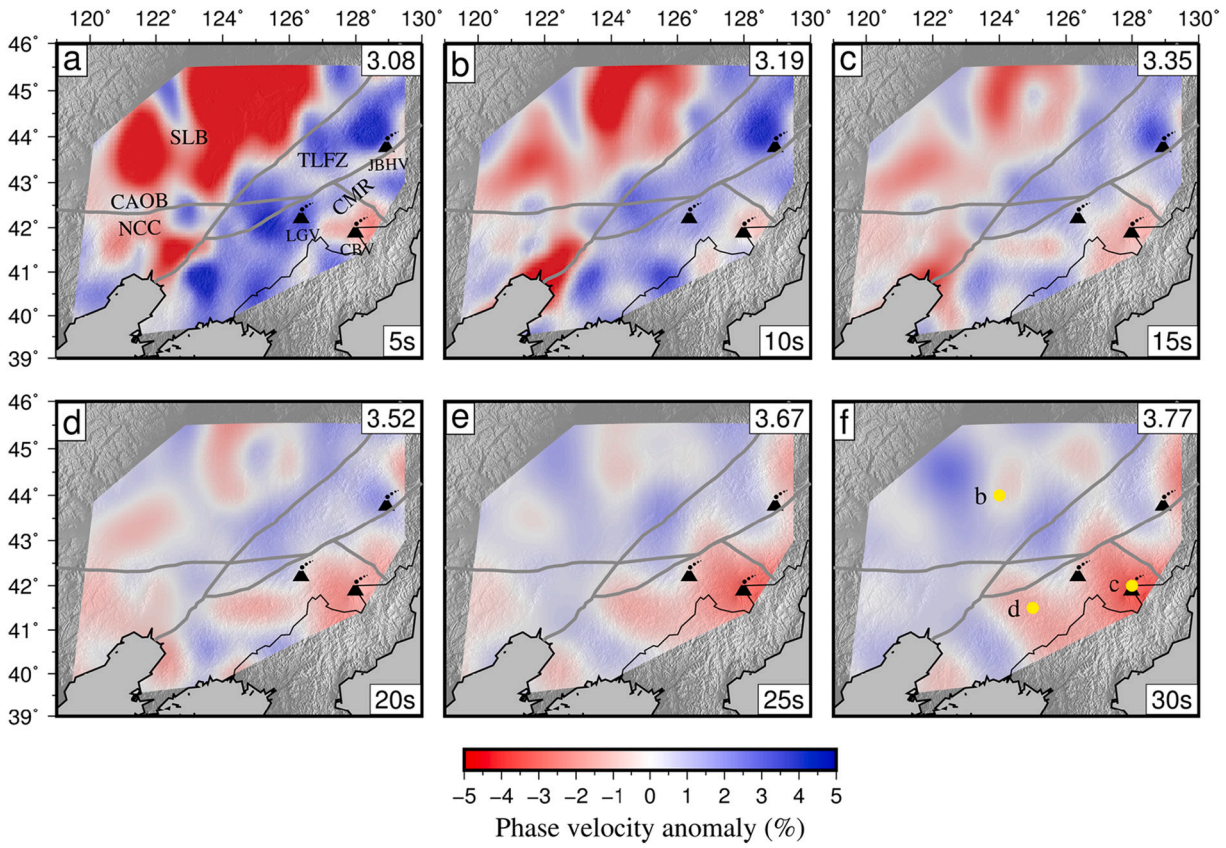

Fig. 7. 2-D phase velocity maps obtained from ambient noise tomography. In each panel, the corresponding period is labeled at the bottom right corner. The anomalies are calculated relative to the average velocity shown in the top right corner of each panel. Volcanoes, tectonic boundaries, faults and other geological features are the same as shown in Fig. 1a. Yellow dots shown in Fig. 7f denote the three geographic locations mentioned in Figs. 8b-d. (For interpretation of the references to colour in this figure legend, the reader is referred to the web version of this article.)

of the NCC is hotter.

6.2. *Cooling of mafic intrusions beneath the southwestern uplift of the SLB*

Many granite samples from the Songliao basin (SLB) give model ages of <1000 Ma (Wu et al., 2000) indicating that the basement consists primarily of young Phanerozoic crust. Our imaging results described here show that the generally lower S wave velocities of the SLB differs from the more ancient crustal velocity structure estimated for the NCC, representing younger crustal age of the CAOB. Therefore, we discuss the crustal velocity structure of the SLB and NCC separately.

The upper and middle crust of the SLB is revealed as a low-velocity feature whose lower Vs range extends to the middle and lower crust. A northwest-trending, high Vs anomaly appears near Tongliao to the southwest (Figs. 9c-d, Fig. 10b). Previous studies and petroleum exploration efforts interpret the SLB as a Mesozoic to Cenozoic basin hosting a mass of sediment which reaches 6 km thick in the central depression (e.g., Wei et al., 2010; Meng et al., 2021). We interpret the low Vs velocity in the upper and middle crust of the SLB as the extreme thick sediments within the basin. A northwest-trending, high-velocity anomaly appears in the southwest of the basin (Fig. 10b) in an area that spatially coincides with the southwest uplift. This uplift divides the basin into a central depression to the northeast and the Kailu sag to the southwest. We interpret the northwest-trending, high Vs anomaly as a subsurface expression of the southwest uplift. The relatively low Vs anomalies on both sides of the uplift indicate sediment infill within the two depressions.

The undulation of the terrain at the Southwest uplift could present the surface high velocity for >10 km (Fig. 10b), but it couldn't explain the high velocity anomaly in middle and lower crust. Geological studies suggest Late Cretaceous mafic dykes were dated at ca. 70 Ma within the southwest uplift (Cheng et al., 2018a). These were formed by partial melting of the depleted lithospheric mantle and incorporation of the lower crust within back-arc extension associated with Pacific plate subduction. Thermochronological studies have found that the basin experienced a rapid cooling and uplift stage related to compression and extension from the Late Cretaceous to Early Paleogene (70–52 Ma) (Cheng et al., 2018b). We therefore conclude that the northwest-trending, high Vs anomaly within the middle and lower crust beneath the southwest uplift likely reflects the addition of mafic material to the crust during the Late Cretaceous.

6.3. *Hot lithospheric mantle underplating the crust beneath NCC*

The Vs appearing in the shallow crust beneath the NCC (Fig. 9a) accords with observed surface geological structures. The TLFZ, Liaodong uplift and Changbai Mountain Range also show large-scale, high-velocity features. The only low Vs anomalies appear locally in the CBV and other major volcanic areas. The Vs of the middle and lower crust varies laterally (Figs. 9c-d). The CBV and Fushun show as low Vs anomalies with about 2% velocity reduction. The two low Vs anomalies merge in the lithospheric mantle to a larger low Vs anomaly (Fig. 10a). Previous studies have also reported a low resistivity and low Vs anomaly in the middle to lower crust beneath the CBV (e.g., Fan and Chen, 2019; Guo et al., 2016; Li et al., 2020). Large-scale tomographic images have reported low Vs characteristics from the Moho to the upper mantle beneath the CBV and a low Vs anomaly extending 400 km to the west (Guo et al., 2016; Tang et al., 2014; Zhang et al., 2019; Zhao et al., 2009). The low Vs anomalies detected in the crust and lithospheric mantle of the CBV and Fushun area accord with these earlier findings.

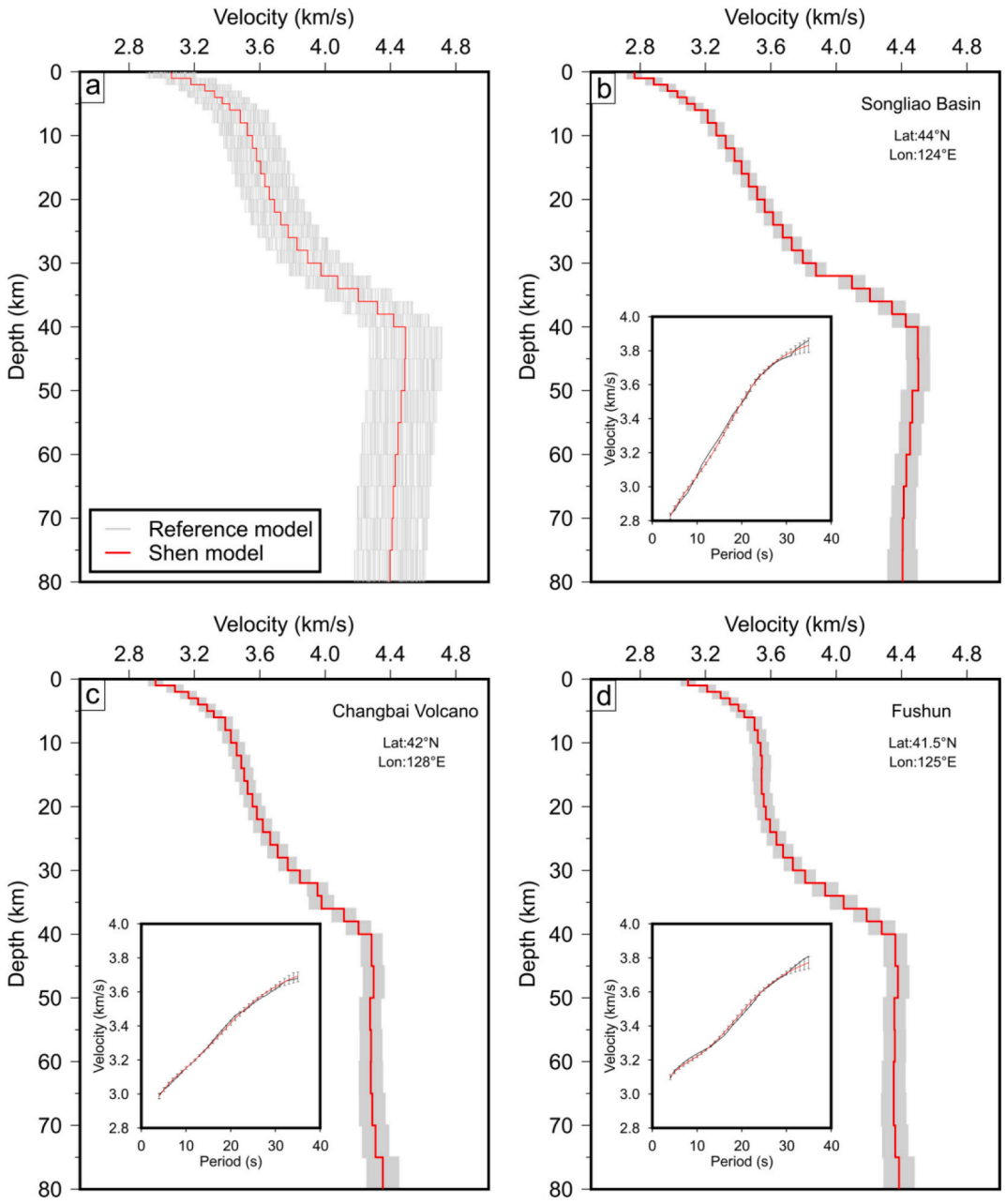

Fig. 8. The inversion results of 1-D S-wave velocity structure beneath the three geographic points denoted in Fig. 7f. (a) The initial input model and relevant 200 derived models. (b-d) Inverted S-wave models at specific locations: b) the SLB, c) the CBV, d) the Fushun, respectively. The red curves in a-d represent the average of all resulting Vs models. The grey areas in a-d show intervals between the two standard deviations for the 200 inverted models. The inset map in each panel demonstrates the comparison of predicted phase velocities (red line) from the best fitting mean model with the observed dispersions (black line). (For interpretation of the references to colour in this figure legend, the reader is referred to the web version of this article.)

Results of previous receiver function studies found that the Moho rests at a deeper level beneath the CBV and Fushun (He et al., 2014; Zhang et al., 2020) relative to the level observed for surrounding areas. Underplating of mantle-derived magma can cause significant subsidence of the Moho surface (Kyong-Song et al., 2016). We therefore interpret the low Vs anomalies beneath the CBV and Fushun as the underplating of hot mantle material formed by partial melting.

In the late Mesozoic and Cenozoic, Northeast China experienced multiple extensional stages (Ren et al., 2002). Kuang et al. (2012) studied Eocene alkaline and tholeiitic rocks in the Laohutai area near Fushun and suggested tholeiites was formed from partial melting of a relatively shallow mantle source (mainly in the stable phase of spinel). This accords with the low Vs anomaly observed in the upper mantle of this area. Receiver function studies detected a shallow Moho discontinuity and a clear offset beneath the TLFZ (Zheng et al., 2015). Electrical detection results meanwhile show that the Yilan-Yitong fault (northern part of the TLFZ) represents a near-vertical, low resistivity zone that penetrates the entire lithosphere (Kaplun et al., 2013). Given frequent volcanic activity along the TLFZ since the Cenozoic (Liu et al., 2001), we speculate that the TLFZ was activated as a channel for upwelling of partially melted mantle material in the early Cenozoic. The Fushun area is situated at the intersection of two branches of the TLFZ, the Dunhua-Mishan and Yilan-Yitong faults. These structures facilitated the underplating of hot, molten mantle-derived materials at the top of the lithosphere and therefore caused partial melting within the middle to lower crust. Therefore, they likely contribute to the low Vs anomaly in the

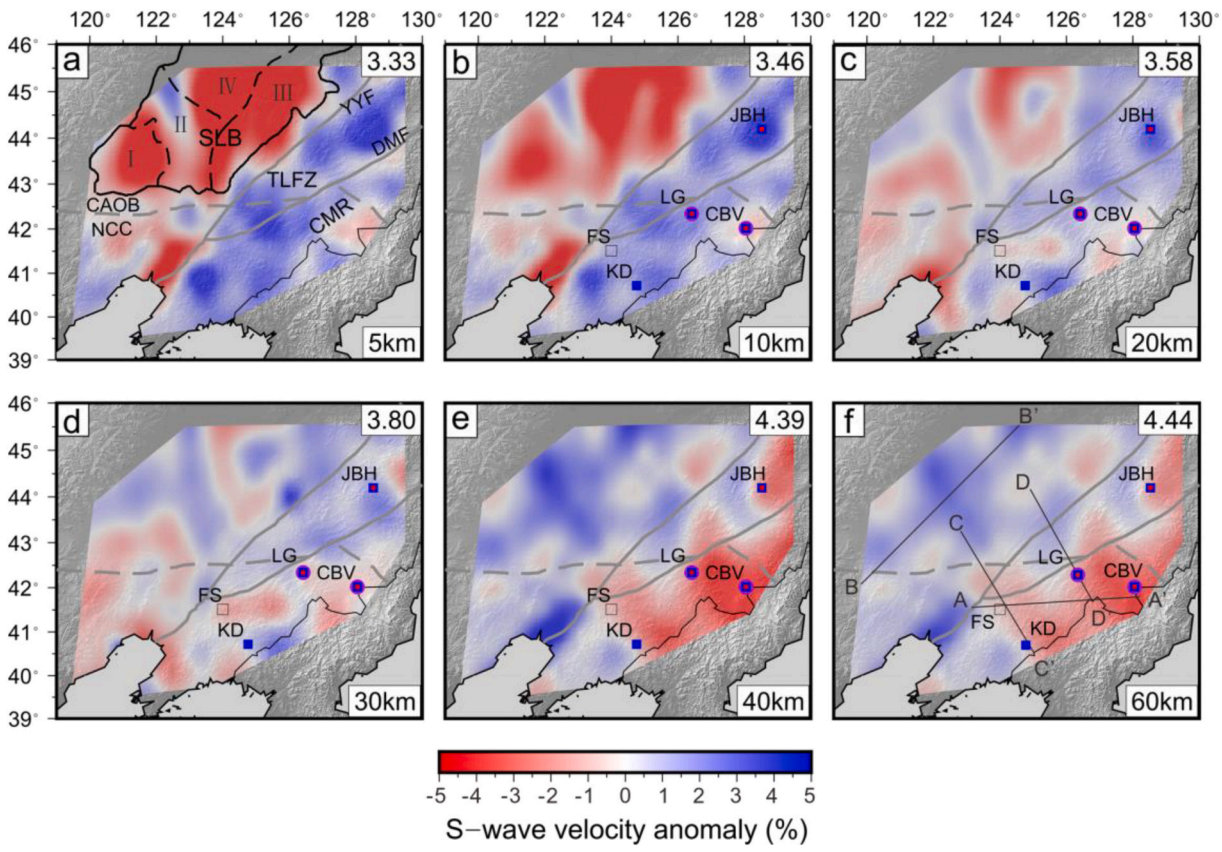

Fig. 9. (a-f) S wave velocity anomaly maps at different depths. The symbols of Cenozoic volcanic basalts age symbols are as follows: Paleocene (black square), Neogene (purple circle), Pleistocene (blue square), and Holocene (red dot). The abbreviations of volcanic basalts area are as follows: Fushun (FS), Kuandian (KD), Longgang (LG), Changbai (CBV) and Jingbohu (JBH) (Modified according to Chen et al. (2007)). Tectonic boundary and sub-tectonic boundaries of the Songliao Basin marked by black line and dashed black lines are shown in Fig. 9a. Four zones are mentioned: I: Kailu sag; II: Southwest Uplift; III: Southeast uplift; IV: Central depression and Western slope. Volcanoes, tectonic boundaries, faults and other geological features are the same as shown in Fig. 1a. In each panel, the corresponding depth is labeled at the bottom right corner. The anomalies are calculated relative to the average values shown in the top right corner of each panel. The profiles of cross-sections A-A′, B-B′, C-C′ and D-D′ in Fig. 10 are delineated in Fig. 9f. (For interpretation of the references to colour in this figure legend, the reader is referred to the web version of this article.)

middle to lower crust of the Fushun detected by imaging results described here (Figs. 9c-d, Fig. 10a, Fig. S1a).

A major middle to lower crustal Vs anomaly and a chamber-like feature within the lithospheric mantle lies beneath the CBV (Figs. 9c-d, Fig. 10a). Previous researchers have speculated that the CBV experienced mantle-derived magmatic underplating and magma accumulation at the middle to lower crustal depths (e.g., Fan and Chen, 2019). Magneto-telluric data shows that the low resistivity anomaly extends from the crust to 150 km beneath the Jingbohu volcano (Li et al., 2021). These works suggest that magma forms as CO_2-rich melts at 150 km depth, then evolves in crustal reservoirs and erupts along conduits. Given the low velocity anomalies in the middle to lower crust and lithospheric mantle beneath the Fushun area, we suggest that Cenozoic basaltic magma could originate from hot, lithospheric mantle melts. This material would thermally erode the lower crust at structurally weaker locations. We interpret anomalies beneath the Fushun and CBV as a lower crustal magma reservoir feeding the volcanoes.

Although no reports have addressed intermediate to acidic volcanics around Fushun, the Kuandian (KD) volcanoes nearby have evolved from volcanoes dominated by alkaline basaltic rocks to one dominated by andesites (Zheng and Zou, 2006). As with the CBV, magma composition shifts from basic to intermediate-acidic. We thus interpret the middle to lower crustal low-velocity body beneath the Fushun and CBV as a shallow magma reservoir, where mantle-derived magma underplates and resides. The low-resistivity zones in the same region are also consistent with the presence of hot melted zones within the crust (Li et al., 2020). Heat flow exhibits an average value of 75.3 $mW \bullet m^{-2}$ near Kuandian (Wang et al., 1988) and 75.4 $mW \bullet m^{-2}$ near the CBV (Jiang et al., 2016). The high values of heat flow further support the interpretation of magma underplating processes. The upper crust beneath the CBV locally exhibits low Vs (Figs. 9a-b). These may record a channel from the middle to lower crustal magma reservoir. Field observations of Kuandian volcanoes indicate magma transfer along major faults acting as conduits. Here the Fushun middle to lower crustal magma reservoir could serve as the magma source.

Seismology, petrology and geochemical results all indicate that the low Vs of the Fushun-Changbai area likely reflects the upwelling of deep hot mantle material as a far-field effect of westward subduction and back-arc extension of the Pacific plate. This process involves partial melting of the SCLM. As they ascend, hot molten magma underplate beneath the Moho along weaker crustal structures. This leads to partial melting of the crust, significant thickening of the crust and low Vs anomalies observed in the middle and lower crust.

7. Conclusion

In this study, we used seismic records from the portable NCISP-10 and NCISP-11 arrays and permanent CEA in Northeast China to construct a 3-D S-wave velocity model for the Liaodong and surrounding areas using ambient noise tomography. The results show that:

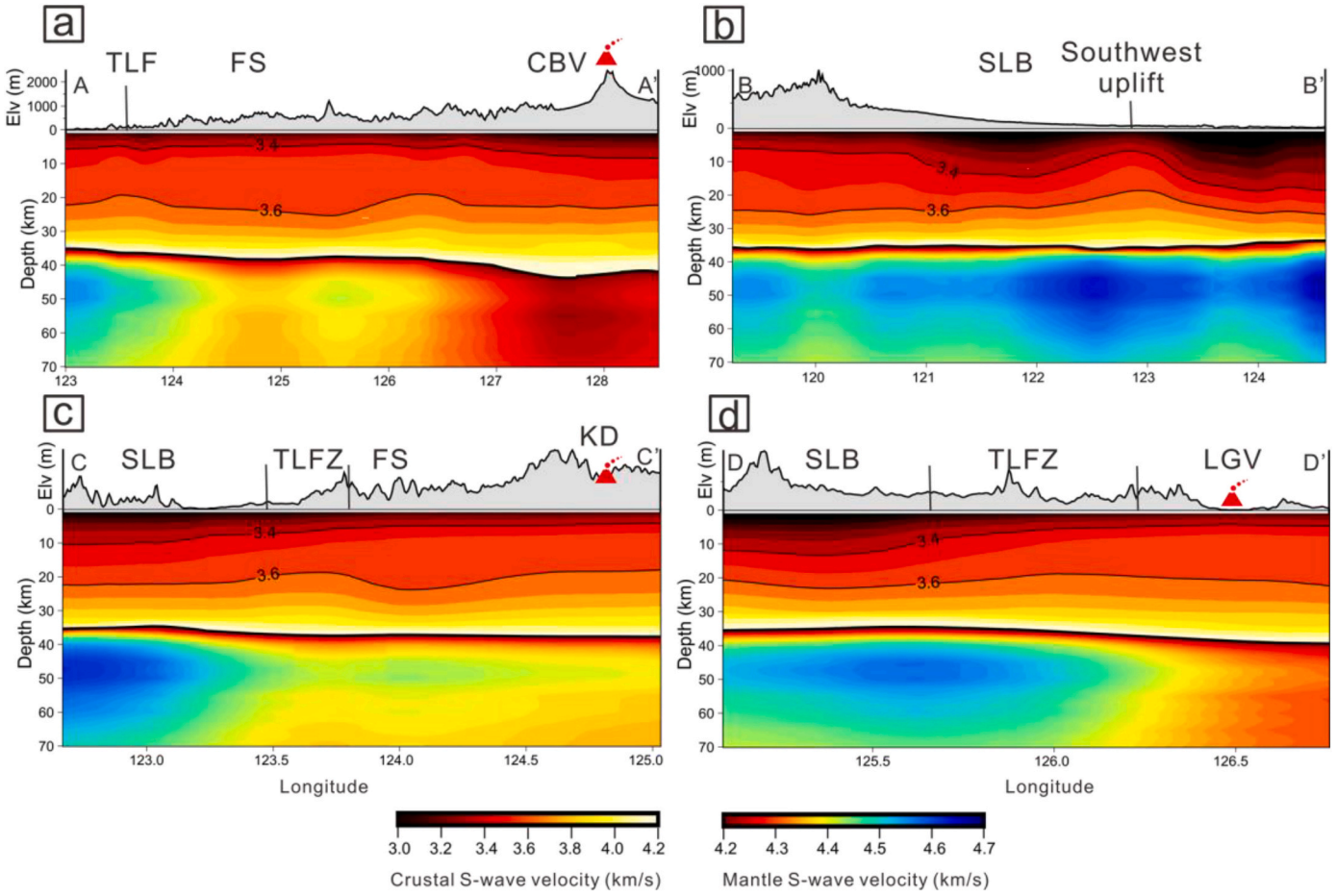

Fig. 10. Vertical cross-sections of S wave velocities along profiles (a) A-A′, (b) B-B′, (c) C-C′ and (d) D-D′ with their profiles shown in Fig. 9f. Surface tomography is plotted on top of each panel. Black curves with values are velocity contours.

(1) A large-scale, low Vs in the upper crust beneath the SLB reveals sedimentary layers with the thickness reaching 10 km. The southwest uplift displays as a high Vs anomaly separating the low Vs anomaly areas of the Kailu sag and central depression. Mafic materials may intrude into the lower crust of the southwest uplift.
(2) The low Vs anomalies in Fushun, CBV and LGV along the northeastern margin of the NCC extend upward from the top of the upper mantle into the middle crust. This accords with current understanding of Cenozoic magmas upwelling from the mantle. Mantle-derived magma underplated beneath the lower crust, resulting in different degrees of partial melting of the lower crust. Subduction of the Pacific plate has eroded parts of the lithospheric mantle of Northeastern China, leading the thinning of lithosphere there, but the degree of thinning varies. The SLB and northeast NCC show as positive and negative velocity anomalies respectively, in the upper mantle, indicating that the NCC have higher temperatures. The higher degree of lithosphere thinning of the NCC may explain this structure contrast between SLB and NCC.

CRediT authorship contribution statement

Lixue Ma: Conceptualization, Methodology, Formal analysis, Investigation, Writing – original draft, Visualization. **Tao Xu:** Validation, Resources, Writing – review & editing, Supervision, Funding acquisition. **Yinshuang Ai:** Data curation, Conceptualization, Resources, Supervision, Validation. **Jinhui Yang:** Funding acquisition. **Yingjie Yang:** Methodology, Software, Writing – review & editing. **Enbo Fan:** Data curation. **Long Li:** Data curation. **Jue Hou:** Data curation. **Weiyu Dong:** Data curation.

Declaration of Competing Interest

The authors declare that they have no known competing financial interests or personal relationships that could have appeared to influence the work reported in this paper.

Data availability

The authors do not have permission to share data.

Acknowledgments

We appreciate the assistance of the IGGCAS Seismic Array Laboratory and the NCISP10 and NCISP11 field team members who collected data for this study, including Drs. Guiping Yu, Guangli Zhang, Haodong Zhang, Fanchang Meng, Minfu Huang and Fan Zheng. We thank the Data Management Center of the China National Seismic Network at the Institute of Geophysics, China Earthquake Administration, for providing seismic data from permanent stations. We are grateful to Profs. Tianyu Zheng, Ling Chen, Laicheng Miao, Huajian Yao, Yonghua Li, Yong Zheng, Youshan Liu for the helpful discussions on data processing and the interpretation of our results. This work is financially supported by the National Natural Science Foundation of China (42130807) and the National Key Research and Development Program of China (2016YFC0600101).

Appendix A. Supplementary data

Supplementary data to this article can be found online at https://doi.org/10.1016/j.tecto.2022.229551.

References

Bensen, G.D., Ritzwoller, M.H., Barmin, M.P., Levshin, A.L., Lin, F., Moschetti, M.P., Shapiro, N.M., Yang, Y., 2007. Processing seismic ambient noise data to obtain reliable broad-band surface wave dispersion measurements. Geophys. J. Int. 169, 1239–1260. https://doi.org/10.1111/j.1365-246X.2007.03374.x.

Chen, Y., Zhang, Y., Graham, D., Su, S., Deng, J., 2007. Geochemistry of Cenozoic basalts and mantle xenoliths in Northeast China. Lithos 96, 108–126. https://doi.org/10.1016/j.lithos.2006.09.015.

Cheng, Y., Li, Ying, Wang, S., Li, Yanfeng, Ao, C., Li, J., Sun, L., Li, H., Zhang, T., 2018a. Late cretaceous tectono–magmatic event in Songliao Basin, NE China: New insights from mafic dyke geochronology and geochemistry analysis. Geol. J. 53, 2991–3008. https://doi.org/10.1002/gj.3137.

Cheng, Y., Wang, S., Li, Ying, Ao, C., Li, Yanfeng, Li, J., Li, H., Zhang, T., 2018b. Late Cretaceous–Cenozoic thermochronology in the southern Songliao Basin, NE China: new insights from apatite and zircon fission track analysis. J. Asian Earth Sci. 160, 95–106. https://doi.org/10.1016/j.jseaes.2018.04.015.

Fan, Q., Hooper, P.R., 1989. The mineral chemistry of ultramafic xenoliths of eastern China: Implications for upper mantle composition and the paleogeotherms. J. Petrol. 30, 1117–1158. https://doi.org/10.1093/petrology/30.5.1117.

Dong, W., Xu, T., Ai, Y., Fan, E., Li, L., Hou, J., 2022. The boundary between the North China Craton and the Central Asian Orogenic Belt in NE China: seismic evidence from receiver function imaging. J. Asian Earth Sci. 237, 105360 https://doi.org/10.1016/j.jseaes.2022.105360.

Fan, X., Chen, Q.F., 2019. Seismic Constraints on the Magmatic System beneath the Changbaishan Volcano: Insight into its Origin and Regional Tectonics. J. Geophys. Res. Solid Earth 124, 2003–2024. https://doi.org/10.1029/2018JB016288.

Feng, Z.Q., Jia, C.Z., Xie, X.N., Zhang, S., Feng, Z.H., Cross, T.A., 2010. Tectonostratigraphic units and stratigraphic sequences of the nonmarine Songliao basin, Northeast China. Basin Res. 22, 79–95. https://doi.org/10.1111/j.1365-2117.2009.00445.x.

Goes, S., Govers, R., Vacher, P., 2000. Shallow mantle temperatures under Europe from P and S wave tomography. J. Geophys. Res. Solid Earth 105, 11153–11169. https://doi.org/10.1029/1999jb900300.

Griffin, W.L., O'Reilly, S.Y., Abe, N., Aulbach, S., Davies, R.M., Pearson, N.J., Doyle, B.J., Kivi, K., 2003. The origin and evolution of Archean lithospheric mantle. Precambrian Res. 127, 19–41. https://doi.org/10.1016/S0301-9268(03)00180-3.

Griot, D.A., Montagner, J.P., Tapponnier, P., 1998. Phase velocity structure from Rayleigh and Love waves in Tibet and its neighboring regions. J. Geophys. Res. Solid Earth 103, 21215–21232. https://doi.org/10.1029/98JB00953.

Guo, Z., Chen, Y.J., Ning, J., Feng, Y., Grand, S.P., Niu, F., Kawakatsu, H., Tanaka, S., Obayashi, M., Ni, J., 2015. High resolution 3-D crustal structure beneath NE China from joint inversion of ambient noise and receiver functions using NECESSArray data. Earth Planet. Sci. Lett. 416, 1–11. https://doi.org/10.1016/j.epsl.2015.01.044.

Guo, Z., Chen, Y.J., Ning, J., Yang, Y., Afonso, J.C., Tang, Y., 2016. Seismic evidence of on-going sublithosphere upper mantle convection for intra-plate volcanism in Northeast China. Earth Planet. Sci. Lett. 433, 31–43. https://doi.org/10.1016/j.epsl.2015.09.035.

Guo, Z., Wang, K., Yang, Y., Tang, Y., John Chen, Y., Hung, S.H., 2018. The Origin and Mantle Dynamics of Quaternary Intraplate Volcanism in Northeast China from Joint Inversion of Surface Wave and Body Wave. J. Geophys. Res. Solid Earth 123, 2410–2425. https://doi.org/10.1002/2017JB014948.

Hao, Y.T., Xia, Q.K., Jia, Z.B., Zhao, Q.C., Li, P., Feng, M., Liu, S.C., 2016. Regional heterogeneity in the water content of the Cenozoic lithospheric mantle of Eastern China. J. Geophys. Res. Solid Earth 121, 517–537. https://doi.org/10.1002/2015JB012105.

He, C., Dong, S., Chen, X., Santosh, M., Niu, S., 2014. Seismic evidence for plume-induced rifting in the Songliao Basin of Northeast China. Tectonophysics 627, 171–181. https://doi.org/10.1016/j.tecto.2013.07.015.

Herrmann, R.B., 2013. Computer programs in seismology: an evolving tool for instruction and research. Seismol. Res. Lett. 84, 1081–1088. https://doi.org/10.1785/0220110096.

Jahn, B.M., Wu, F., Chen, B., 2000. Massive granitoid generation in Central Asia: Nd isotope evidence and implication for continental growth in the Phanerozoic. Episodes 23, 82–92. https://doi.org/10.18814/epiiugs/2000/v23i2/001.

Jiang, G.Z., Gao, P., Rao, S., Zhang, L.Y., Tang, X.Y., Huang, F., Zhao, P., Pang, Z.H., He, L.J., Hu, S.B., Wang, J.Y., 2016. Compilation of heat flow data in the continental area of China (4th edition). Acta Geophys. Sin. 59, 2892–2910. https://doi.org/10.6038/cjg20160815.

Kaplun, V.B., Kirillova, G.L., Tonglin, L.I., 2013. Geoelectrical structures of northern segment of Tan-Lu fault system in China and Russia areas based on magnetotelluric soundings. Global Geol. 16, 164–174.

Karato, S.I., 2011. Water distribution across the mantle transition zone and its implications for global material circulation. Earth Planet. Sci. Lett. 301, 413–423. https://doi.org/10.1016/j.epsl.2010.11.038.

Kuang, Y.S., Wei, X., Hong, L.B., Ma, J.L., Pang, C.J., Zhong, Y.T., Zhao, J.X., Xu, Y.G., 2012. Petrogenetic evaluation of the Laohutai basalts from North China Craton: Melting of a two-component source during lithospheric thinning in the late Cretaceous-early Cenozoic. Lithos 154, 68–82. https://doi.org/10.1016/j.lithos.2012.06.027.

Kyong-Song, R., Hammond, J.O.S., Chol-Nam, K., Hyok, K., Yong-Gun, Y., Gil-Jong, P., Chong-Song, R., Oppenheimer, C., Liu, K.W., Iacovino, K., Kum-Ran, R., 2016. Evidence for partial melt in the crust beneath Mt. Paektu (Changbaishan), Democratic People's Republic of Korea and China. Sci. Adv. 2, e1501513 https://doi.org/10.1126/sciadv.1501513.

Lei, J., Zhao, D., 2005. P-wave tomography and origin of the Changbai intraplate volcano in Northeast Asia. Tectonophysics 397, 281–295. https://doi.org/10.1016/j.tecto.2004.12.009.

Levshin, A.L., Ritzwoller, M.H., 2001. Automated detection, extraction, and measurement of regional surface waves. Pure Appl. Geophys. 158, 1531–1545. https://doi.org/10.1007/pl00001233.

Li, S., Weng, A., Li, J., Shan, X., Han, J., Tang, Y., Zhang, Y., Wang, X., 2020. Deep origin of Cenozoic volcanoes in Northeast China revealed by 3-D electrical structure. Sci. China Earth Sci. 63, 533–547. https://doi.org/10.1007/s11430-018-9537-2.

Li, Y., Weng, A., Xu, W., Zou, Z., Tang, Y., Zhou, Z., Li, S., Zhang, Y., Ventura, G., 2021. Translithospheric magma plumbing system of intraplate volcanoes as revealed by electrical resistivity imaging. Geology 49, 1337–1342. https://doi.org/10.1130/G49032.1.

Li, Z., Li, Y., Zheng, J.P., Han, D., 2007. Late Mesozoic tectonic transition of the eastern North China Craton: evidence from basin-fill records. Geol. Soc. Spec. Publ. 280, 239–266. https://doi.org/10.1144/SP280.12.

Liu, D.Y., Nutman, A.P., Compston, W., Wu, J.S., Shen, Q.H., 1992. Remnants of ≥3800 Ma crust in the Chinese part of the Sino- Korean craton. Geology 20, 339–342. https://doi.org/10.1130/0091-7613(1992)020<0339:ROMCIT>2.3.CO;2.

Liu, J., Han, J., Fyfe, W.S., 2001. Cenozoic episodic volcanism and continental rifting in Northeast China and possible link to Japan Sea development as revealed from K-Ar geochronology. Tectonophysics 339, 385–401. https://doi.org/10.1016/S0040-1951(01)00132-9.

Liu, J., Shen, L., Ji, M., Guan, H., Zhang, Z., Zhao, Z., 2013. The Liaonan/Wanfu metamorphic core complexes in the Liaodong Peninsula: two stages of exhumation and constraints on the destruction of the North China Craton. Tectonics 32, 1121–1141. https://doi.org/10.1002/tect.20064.

Liu, R., Xie, G., Zhou, X., Chen, W., Fan, Q., 1995. Tectonic environments of Cenozoic volcanic rocks in China and characteristics of the source regions in the mantle. Chin. J. Geochem. 14, 289–302. https://doi.org/10.1007/BF02872628.

Liu, Y., Niu, F., Chen, M., Yang, W., 2017. 3-D crustal and uppermost mantle structure beneath NE China revealed by ambient noise adjoint tomography. Earth Planet. Sci. Lett. 461, 20–29. https://doi.org/10.1016/j.epsl.2016.12.029.

Meng, F., Ai, Y., Xu, T., Chen, L., Wang, X., Li, L., 2021. Lithospheric structure beneath the boundary region of North China Craton and Xing Meng Orogenic Belt from S-receiver function analysis. Tectonophysics 818, 229067. https://doi.org/10.1016/j.tecto.2021.229067.

Meng, Q.R., Hu, J.M., Jin, J.Q., Zhang, Y., Xu, D.F., 2003. Tectonics of the late Mesozoic wide extensional basin system in the China-Mongolia border region. Basin Res. 15, 397–415. https://doi.org/10.1046/j.1365-2117.2003.00209.x.

Montagner, J.P., Nataf, H.C., 1986. A simple method for inverting the azimuthal anisotropy of surface waves. J. Geophys. Res. 91, 511–520. https://doi.org/10.1029/JB091iB01p00511.

Nafe, J.E., Drake, C.L., 1957. Variation with depth in shallow and deep water marine sediments of porosity, density and the velocities of compressional and shear waves. Geophysics 22, 523–552. https://doi.org/10.1190/1.1438386.

O'Reilly, S.Y., Griffin, W.L., 2006. Imaging global chemical and thermal heterogeneity in the subcontinental lithospheric mantle with garnets and xenoliths: Geophysical implications. Tectonophysics 416, 289–309. https://doi.org/10.1016/j.tecto.2005.11.014.

Ren, J., Tamaki, K., Li, S., Junxia, Z., 2002. Late Mesozoic and Cenozoic rifting and its dynamic setting in Eastern China and adjacent areas. Tectonophysics 344, 175–205. https://doi.org/10.1016/S0040-1951(01)00271-2.

Shen, W.S., Ritzwoller, M.H., Kang, D., Kim, Y., Lin, F.C., Ning, J.Y., 2016. A seismic reference model for the crust and uppermost mantle beneath China from surface wave dispersion. Geophys. J. Int. 206, 954–979. https://doi.org/10.1093/gji/ggw175.

Song, Y., Ren, J., Stepashko, A.A., Li, J., 2014. Post-rift geodynamics of the Songliao Basin, NE China: Origin and significance of T11 (Coniacian) unconformity. Tectonophysics 634, 1–18. https://doi.org/10.1016/j.tecto.2014.07.023.

Song, Y., Ren, J., Liu, K., Shen, C., Stepashko, A., 2018. Post-rift anomalous thermal flux in the Songliao Basin, NE China, as revealed from fission track thermochronology and tectonic analysis. Palaeogeogr. Palaeoclimatol. Palaeoecol. 508, 148–165. https://doi.org/10.1016/j.palaeo.2018.07.030.

Tang, J., Xu, W., Wang, F., Ge, W., 2018. Subduction history of the Paleo-Pacific slab beneath Eurasian continent: Mesozoic-Paleogene magmatic records in Northeast Asia. Sci. China Earth Sci. 61, 527–559. https://doi.org/10.1007/s11430-017-9174-1.

Tang, Y., Obayashi, M., Niu, F., Grand, S.P., Chen, Y.J., Kawakatsu, H., Tanaka, S., Ning, J., Ni, J.F., 2014. Changbaishan volcanism in Northeast China linked to subduction-induced mantle upwelling. Nat. Geosci. 7, 470–475. https://doi.org/10.1038/ngeo2166.

Tang, Y.J., Zhang, H.F., Ying, J.F., Su, B.X., 2013. Widespread refertilization of cratonic and circum-cratonic lithospheric mantle. Earth Sci. Rev. 118, 45–68. https://doi.org/10.1016/j.earscirev.2013.01.004.

Tao, K., Niu, F., Ning, J., Chen, Y.J., Grand, S., Kawakatsu, H., Tanaka, S., Obayashi, M., Ni, J., 2014. Crustal structure beneath NE China imaged by NECESSArray receiver function data. Earth Planet. Sci. Lett. 398, 48–57. https://doi.org/10.1016/j.epsl.2014.04.043.

Wang, A., Ren, Y., Sun, W., Yu, L., Liang, J., Cao, T., Gu, H., 1988. Geothermal observations in East Liaoning and Haicheng seismic area. Acta Seismol. Sin. 1, 60–72. https://doi.org/10.1007/BF02652411.

Wang, C., Feng, Z., Zhang, L., Huang, Y., Cao, K., Wang, P., Zhao, B., 2013. Cretaceous paleogeography and paleoclimate and the setting of SKI borehole sites in Songliao Basin, Northeast China. Palaeogeogr. Palaeoclimatol. Palaeoecol. 385, 17–30. https://doi.org/10.1016/j.palaeo.2012.01.030.

Wang, H., Mo, X., 1995. An outline of the tectonic evolution of China. Episodes 18, 6–16. https://doi.org/10.18814/epiiugs/1995/v18i1.2/003.

Wei, H.H., Liu, J.L., Meng, Q.R., 2010. Structural and sedimentary evolution of the southern Songliao Basin, Northeast China, and implications for hydrocarbon prospectivity. Am. Assoc. Pet. Geol. Bull. 94, 533–566. https://doi.org/10.1306/09080909060.

Wu, F. Yuan, Sun, D. You, Li, H., Jahn, B. Ming, Wilde, S., 2002. A-type granites in northeastern China: Age and geochemical constraints on their petrogenesis. Chem. Geol. 187, 143–173. https://doi.org/10.1016/S0009-2541(02)00018-9.

Wu, F. Yuan, Walker, R.J., Ren, X. Wen, Sun, D. You, Hua, Zhou X., 2003. Osmium isotopic constraints on the age of lithospheric mantle beneath northeastern China. Chem. Geol. 196, 107–129. https://doi.org/10.1016/S0009-2541(02)00409-6.

Wu, F., Ge, W., Sun, D., Lin, Q., Zhou, Y., 1997. The Sm-Nd, Rb-Sr isotopic ages of the Archean granites in southern Jilin Province. Acta Petrol. Sin. 13, 499–506.

Wu, F.Y., Jahn, B.M., Wilde, S., Sun, D.Y., 2000. Phanerozoic crustal growth: U-Pb and Sr-Nd isotopic evidence from the granites in northeastern China. Tectonophysics 328, 89–113. https://doi.org/10.1016/S0040-1951(00)00179-7.

Yang, Y., Ritzwoller, M.H., Levshin, A.L., Shapiro, N.M., 2007. Ambient noise Rayleigh wave tomography across Europe. Geophys. J. Int. 168, 259–274. https://doi.org/10.1111/j.1365-246X.2006.03203.x.

Yao, H., van der Hilst, R.D., Montagner, J.P., 2010. Heterogeneity and anisotropy of the lithosphere of SE Tibet from surface wave array tomography. J. Geophys. Res. Solid Earth 115, B12307. https://doi.org/10.1029/2009JB007142.

Yu, S.Y., Xu, Y.G., Huang, X.L., Ge, W.C., Cheng, J., 2007. Comparison of composition and thermal state of the upper mantle beneath northeast and North China: Implications for lithospheric thinning in eastern China. Acta Petrol. Sin. 23, 1252–1268.

Zhang, B., Zhu, G., Jiang, D., Li, C., Chen, Y., 2012. Evolution of the Yiwulushan metamorphic core complex from distributed to localized deformation and its tectonic implications. Tectonics 31, TC4018. https://doi.org/10.1029/2012TC003104.

Zhang, B., Lei, J., Yuan, X., Zhang, G., He, J., Xu, Q., 2020. Detailed Moho variations under Northeast China inferred from receiver function analyses and their tectonic implications. Phys. Earth Planet. Inter. 300, 106448 https://doi.org/10.1016/j.pepi.2020.106448.

Zhang, F., Wu, Q., Li, Y., Zhang, R., 2019. The seismic evidence of velocity variation for Changbaishan volcanism in Northeast China. Geophys. J. Int. 218, 283–294. https://doi.org/10.1093/gji/ggz157.

Zhang, S.H., Zhao, Y., Davis, G.A., Ye, H., Wu, F., 2014. Temporal and spatial variations of Mesozoic magmatism and deformation in the North China Craton: Implications for lithospheric thinning and decratonization. Earth Sci. Rev. 131, 49–87. https://doi.org/10.1016/j.earscirev.2013.12.004.

Zhao, D., Tian, Y., 2013. Changbai intraplate volcanism and deep earthquakes in east asia: a possible link? Geophys. J. Int. 195, 706–724. https://doi.org/10.1093/gji/ggt289.

Zhao, D., Tian, Y., Lei, J., Liu, L., Zheng, S., 2009. Seismic image and origin of the Changbai intraplate volcano in East Asia: Role of big mantle wedge above the stagnant Pacific slab. Phys. Earth Planet. Inter. 173, 197–206. https://doi.org/10.1016/j.pepi.2008.11.009.

Zheng, R.L., Zou, T.R., 2006. Geological characteristics and its particularity of Kuandian Volcano group in Niaoling Province. Geol. Resourc. 15, 75–77.

Zheng, T.Y., He, Y.M., Yang, J.H., Zhao, L., 2015. Seismological constraints on the crustal structures generated by continental rejuvenation in northeastern China. Sci. Rep. 5, 14995 https://doi.org/10.1038/srep14995.

Zheng, X.F., Yao, Z.X., Liang, J.H., Zheng, J., 2010. The role played and opportunities provided by igp dmc of China national seismic network in wenchuan earthquake disaster relief and researches. Bull. Seismol. Soc. Am. 100, 2866–2872. https://doi.org/10.1785/0120090257.

Zhu, G., Jiang, D., Zhang, B., Chen, Y., 2012. Destruction of the eastern North China Craton in a backarc setting: evidence from crustal deformation kinematics. Gondwana Res. 22, 86–103. https://doi.org/10.1016/j.gr.2011.08.005.